AIP | Review of Scientific Instruments

Simulating and interpreting Kelvin probe force microscopy images on dielectrics with boundary integral equations

Yongxing Shen, David M. Barnett, and Peter M. Pinsky

Citation: Rev. Sci. Instrum. **79**, 023711 (2008); doi: 10.1063/1.2885679
View online: http://dx.doi.org/10.1063/1.2885679
View Table of Contents: http://rsi.aip.org/resource/1/RSINAK/v79/i2
Published by the American Institute of Physics.

Simulating and interpreting Kelvin probe force microscopy images on dielectrics with boundary integral equations

Yongxing Shen,[1,a)] David M. Barnett,[1,b)] and Peter M. Pinsky[2]
[1]*Department of Materials Science and Engineering, Stanford University, Stanford, California 94305, USA*
[2]*Department of Mechanical Engineering, Stanford University, Stanford, California 94305, USA*

(Received 17 August 2007; accepted 4 February 2008; published online 28 February 2008)

Kelvin probe force microscopy (KPFM) is designed for measuring the tip-sample contact potential differences by probing the sample surface, measuring the electrostatic interaction, and adjusting a feedback circuit. However, for the case of a dielectric (insulating) sample, the contact potential difference may be ill defined, and the KPFM probe may be sensing electrostatic interactions with a certain distribution of sample trapped charges or dipoles, leading to difficulty in interpreting the images. We have proposed a general framework based on boundary integral equations for simulating the KPFM image based on the knowledge about the sample charge distributions (forward problem) and a deconvolution algorithm solving for the trapped charges on the surface from an image (inverse problem). The forward problem is a classical potential problem, which can be efficiently solved using the boundary element method. Nevertheless, the inverse problem is ill posed due to data incompleteness. For some special cases, we have developed deconvolution algorithms based on the forward problem solution. As an example, this algorithm is applied to process the KPFM image of a gadolinia-doped ceria thin film to solve for its surface charge density, which is a more relevant quantity for samples of this kind than the contact potential difference (normally only defined for conductive samples) values contained in the raw image. © *2008 American Institute of Physics.*
[DOI: 10.1063/1.2885679]

I. INTRODUCTION

Kelvin probe force microscopy (KPFM) was invented by Nonnenmacher *et al.*[1] as a special design of electrostatic force microscopy for measuring the sample contact potential difference (CPD). It has been applied to characterize various types of solids used in electronic devices such as ionic crystal thin films,[2] semiconductors,[3] organic solar cell structures,[4] and nanographenes[5] in order to study the sample lateral variations of surface potentials and work functions and infer the electronic structures.

However, detailed analysis shows that an image obtained with KPFM is only an approximation to the actual sample surface potential due to the finite curvature of the probe tip and the long-range characteristic of the Coulombic interaction. In their model,[6] Jacobs *et al.* treated the sample as a multiconductor system, of which each of the constituent conductor has its own potential Φ_i and forms a capacitor with the probe tip, C_{it}. The KPFM signal of a particular configuration (i.e., a particular probe tip position) is the weighted average of all the Φ_i's, the weights being the derivative of C_{it} with respect to the tip-sample separation. While the conductor potentials are assumed to be fixed, the weights are functions of the tip position. Under the assumption of a flat sample and a constant tip-sample separation and in the limit of *continuous* CPD variation, the KPFM image becomes a two-dimensional convolution of the "true" surface potential variation and a response function (also called a *transfer function*).

Such a convolution relation permits solving for the true sample surface potential by deconvolution. For example, Strassburg *et al.*[7] have developed a deconvolution algorithm for the special case of flat conductive samples. This development has employed the boundary integral equation approach with an image source in Green's function to model the electrostatics, and the sample is assumed to have a fixed surface dipole layer that is solely responsible for the interaction with the KPFM probe. The response function is computed via the boundary element method in an efficient and robust way, and the deconvolution is performed in combination with certain extrapolation (not stated) and a Wiener filter to mitigate the edge effect and the instrument noise, respectively.

While Strassburg *et al.*[7] have established a systematic methodology for reconstructing surface potentials from KPFM images of flat conductive samples, a counterpart treatment for another class of practically important materials—dielectrics (insulators)—still does not exist. An example of such materials is ionic crystals,[2] which are widely used in electronic devices and thus deserve a detailed model for studying their KPFM measurements.

In this work, we will generalize the framework of Strassburg *et al.*[7] for solving both the forward (predicting the image from the prescribed charge distributions) and inverse (solving the charge distributions from the image) problems for dielectrics. In the case of a flat sample surface and a homogeneous isotropic dielectric constant, the counterpart

[a)]Electronic mail: shenyx@stanford.edu.
[b)]Also at Department of Mechanical Engineering, Stanford University.

boundary integral equation can be derived using Green's function with an appropriate image source term.

On the other hand, the inverse problem for dielectrics will be shown to be ill posed because of insufficient data, which requires additional information about the material property and its treatment history, e.g., surface modulation that the sample has undergone, in order to obtain a meaningful solution. If the sample can be described by containing either only a surface dipole layer or only a surface trapped charge layer, analogous deconvolution algorithms can be employed to solve for the assumed layer of source. Sample application of this methodology to raw experimental data will be illustrated.

II. IMAGING MECHANISM OF KPFM

A. Imaging mechanism derived from the model of a simple capacitor

KPFM was originally designed for detecting local CPD between a *conductive* sample and the tip. This apparatus consists of an atomic force microscope (AFM) and a control circuit. The KPFM scan is usually performed following a topographic scan by the AFM. After obtaining the sample surface topography, the AFM probe tip is lifted above the sample to some separation and is controlled to scan the sample by tracing the topography obtained from the previous scan. In the mean time, a voltage V with both direct current (dc) and alternating current (ac) components is applied to the probe,

$$V = V_{\mathrm{dc}} + V_{\mathrm{ac}} \sin(\omega t), \tag{1}$$

where t denotes time and ω is the angular frequency of the ac voltage.

Let Φ denote the tip-sample CPD; then if Φ does not vary significantly at different locations, the system electrostatic energy can be *approximated* as

$$W = \tfrac{1}{2} C (V - \Phi)^2, \tag{2}$$

where C is the probe-sample capacitance (strictly speaking, the capacitance between the sample and the entire cantilever with the probe). The attractive capacitive force is then given by

$$F = -\frac{\partial W}{\partial z}, \tag{3}$$

where z is the probe-sample separation. Substituting Eqs. (1) and (2) into Eq. (3) yields

$$F = -\frac{1}{2}\frac{\partial C}{\partial z}[V_{\mathrm{dc}} + V_{\mathrm{ac}} \sin(\omega t) - \Phi]^2. \tag{4}$$

Expanding Eq. (4) and grouping terms in terms of their time dependence, F can be decomposed as

$$F = F_{\mathrm{dc}} + F_{\omega} \sin(\omega t) + F_{2\omega} \cos(2\omega t), \tag{5}$$

where

$$F_{\mathrm{dc}} = -\frac{1}{2}\frac{\partial C}{\partial z}\left[(V_{\mathrm{dc}} - \Phi)^2 + \frac{1}{2}V_{\mathrm{ac}}^2\right], \tag{6}$$

$$F_{\omega} = -\frac{\partial C}{\partial z} V_{\mathrm{ac}} (V_{\mathrm{dc}} - \Phi), \tag{7}$$

$$F_{2\omega} = \frac{1}{4}\frac{\partial C}{\partial z} V_{\mathrm{ac}}^2. \tag{8}$$

These components can be obtained individually using the control circuit, which is essentially obtaining a particular Fourier component by utilizing their orthogonality (strictly speaking, it is the cantilever oscillation amplitudes that are being recorded).

Note that in this model, $F_{\omega}=0$ if and only if $V_{\mathrm{dc}}=\Phi$. By adjusting V_{dc} using the feedback circuit to nullify F_{ω}, one is able to measure Φ by recording V_{dc}. (In reality, it is the cantilever's oscillation amplitude at frequency ω that is being zeroed. Moreover, because of the unavoidable thermal fluctuation, the amplitude is never zero; thus, nullification is replaced with minimization.[8] In this work, however, we will neglect these errors for simplicity.) Such an operation is performed for each sampling point on the sample surface before the tip is translated to the next position. All these V_{dc} values constitute the KPFM image, which is assumed to provide the spatial variation of the CPD Φ.

B. Limitations of the model of a simple capacitor

The KPFM image obtained via the imaging mechanism described above is, however, only an approximation to the actual CPD between a tip and a conductive sample. This is because Eq. (2) is exact only when Φ is constant over the sample surface; otherwise, the tip-sample system is no longer a simple capacitor.

On the other hand, some materials, especially dielectrics, may possess a surface *charge* layer, a surface *dipole* layer, or interior charges, or any combination of these cases. Such samples may not have a well-defined CPD. When they interact with the KPFM, their surface charges, surface dipoles, and interior charges all participate in the overall Coulombic interaction.

Thus, a model that takes into account these possible charge/dipole distributions is needed for the forward problem of predicting the KPFM image under certain experimental conditions and for the inverse problem of solving for such charge/dipole distributions from a KPFM image.

III. BOUNDARY INTEGRAL EQUATION MODELING FOR THE FORWARD PROBLEM

For the forward problem, we shall start with the boundary value problem that describes the probe-sample interaction and transform it to the equivalent boundary integral equation in order to solve for the electric field and predict the KPFM signal.

A. Electrostatic boundary value problem

Judging from the dimensions of the problem, we can apply the quasistatic approximation despite the time-dependent voltage applied between the probe tip and the sample. This approximation allows us to neglect the magnetic field and to use a scalar potential ϕ such that $-\nabla\phi$

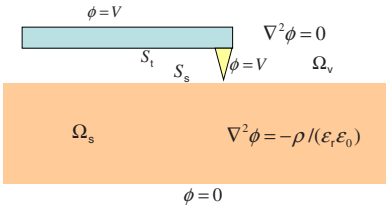

FIG. 1. (Color online) Schematic of the electrostatic boundary value problem involved in KPFM.

$=\mathbf{E}$, where $\mathbf{E}$ is the electric field. The KPFM cantilever with the probe tip is assumed to be a perfect conductor, whose potential is a constant given by Eq. (1). The sample is assumed to be semi-infinite with a flat surface and an isotropic homogeneous dielectric constant ε_r. A conductive sample can be treated as a special case in which $\varepsilon_r \to \infty$.

The electrostatics involved in KPFM can be described by these governing partial differential equations: Poisson's equation in the sample interior and Laplace's equation in the open space (vacuum) outside the probe tip and the sample, i.e.,

$$\nabla^2\phi = \begin{cases} -\rho/(\varepsilon_r\varepsilon_0) & \text{in} \quad \Omega_s \\ 0 & \text{in} \quad \Omega_v, \end{cases} \tag{9}$$

where ∇^2 is the Laplacian operator, ρ is the trapped sample volumetric charge density, $\varepsilon_0 = 8.8542 \times 10^{-12}$ F/m is the vacuum permittivity, and Ω_v and Ω_s are the volumetric domains of the open space and the sample, respectively.

The boundary value problem governed by Eq. (9) is a two-domain problem with a boundary condition on the surface of (the cantilever plus the probe tip) S_t,

$$\phi = V \quad \text{on } S_t, \tag{10}$$

and two continuity conditions across the sample surface S_s,

$$\phi_s - \phi_v = -\Phi \quad \text{and} \quad \varepsilon_r\varepsilon_0 \frac{\partial\phi_s}{\partial\mathbf{n}} - \varepsilon_0 \frac{\partial\phi_v}{\partial\mathbf{n}} = \Sigma \quad \text{on } S_s, \tag{11}$$

where subscripts v and s denote whether the values are evaluated on the vacuum side or the sample side, $\mathbf{n}$ is the outward surface normal of the sample, and Φ and Σ are the sample surface dipole layer (double layer) density and charge (single layer) density, respectively. A schematic of the boundary value problem is shown in Fig. 1.

B. Boundary integral equation

If the sample surface S_s is flat, a boundary integral equation equivalent to this boundary value problem can be derived from Green's second identity as (see Appendix A)

$$\int_{S_t} \tilde{G}(\mathbf{r};\mathbf{r}')\sigma(\mathbf{r})dS(\mathbf{r}) = V - V_\Phi(\mathbf{r}') - V_\Sigma(\mathbf{r}') - V_\rho(\mathbf{r}'), \quad \forall\, \mathbf{r}' \in S_t, \tag{12}$$

where the primary unknown function is $\sigma(\mathbf{r})$, the induced surface charge density on the probe tip, which is related to the electric field magnitude immediately outside the conductive probe as $\sigma = \varepsilon_0 E$. The integral kernel of Eq. (12) is

$$\tilde{G}(\mathbf{r};\mathbf{r}') \equiv G(\mathbf{r}-\mathbf{r}') - \frac{\varepsilon_r - 1}{\varepsilon_r + 1} G(\mathbf{r} - \overline{\mathbf{r}'}), \tag{13}$$

where $G(\mathbf{r}-\mathbf{r}') \equiv (4\pi\varepsilon_0|\mathbf{r}-\mathbf{r}'|)^{-1}$ is the free space Green's function for electrostatics with field point $\mathbf{r}$ and source point $\mathbf{r}'$, and $\overline{\mathbf{r}'}$ is the mirror image position of $\mathbf{r}'$ with respect to S_s.

V_Φ, V_Σ, and V_ρ denote the individual contributions from Φ, Σ, and ρ, respectively,

$$V_\Phi(\mathbf{r}') \equiv \frac{2\varepsilon_r\varepsilon_0}{\varepsilon_r + 1} \int_{S_s} \frac{\partial G(\mathbf{r}-\mathbf{r}')}{\partial\mathbf{n}_\mathbf{r}} \Phi(\mathbf{r})dS(\mathbf{r}), \tag{14}$$

$$V_\Sigma(\mathbf{r}') \equiv \frac{2}{\varepsilon_r + 1} \int_{S_s} G(\mathbf{r}-\mathbf{r}')\Sigma(\mathbf{r})dS(\mathbf{r}), \tag{15}$$

$$V_\rho(\mathbf{r}') \equiv \frac{2}{\varepsilon_r + 1} \int_{\Omega_s} G(\mathbf{r}-\mathbf{r}')\rho(\mathbf{r})d\Omega(\mathbf{r}). \tag{16}$$

Equation (12) is a Fredholm integral equation of the first kind. For the case of a conductive sample, we can let $\varepsilon_r \to \infty$ so that Eq. (12) reduces to

$$\int_{S_t} \tilde{G}(\mathbf{r};\mathbf{r}')\sigma(\mathbf{r})dS(\mathbf{r}) = V - 2\varepsilon_0 \int_{S_s} \frac{\partial G(\mathbf{r}-\mathbf{r}')}{\partial\mathbf{n}_\mathbf{r}} \Phi(\mathbf{r})dS(\mathbf{r}), \quad \forall\, \mathbf{r}' \in S_t, \tag{17}$$

where

$$\tilde{G}(\mathbf{r};\mathbf{r}') = G(\mathbf{r}-\mathbf{r}') - G(\mathbf{r} - \overline{\mathbf{r}'}). \tag{18}$$

Equation (17) agrees with the formulation of Ref. 7.

The implementation of the boundary element method for solving Eq. (12) is given in Appendix B. For notational simplicity, we define $\tilde{G}^{-1}(\mathbf{r}'';\mathbf{r}')$ as the inverse of the kernel $\tilde{G}(\mathbf{r};\mathbf{r}')$ such that

$$\int_{S_t} \tilde{G}^{-1}(\mathbf{r}'';\mathbf{r}')\tilde{G}(\mathbf{r};\mathbf{r}')dS(\mathbf{r}) = \delta(\mathbf{r}-\mathbf{r}''), \quad \forall\, \mathbf{r} \in S_t, \quad \mathbf{r}'' \in S_t, \tag{19}$$

where δ is the two-dimensional Dirac delta function with respect to S_t. From now on, $\tilde{G}^{-1}(\mathbf{r}'';\mathbf{r}')$ is assumed to be known, and we can formally invert Eq. (12) by multiplying $\tilde{G}^{-1}(\mathbf{r}'';\mathbf{r}')$ on both sides of Eq. (12) and integrate over S_t with respect to $\mathbf{r}'$. Then, σ can be written as the sum of contributions from the individual sources V, Φ, Σ, and ρ,

$$\sigma = V\sigma_1 - \sigma_\Phi - \sigma_\Sigma - \sigma_\rho, \tag{20}$$

where

$$\sigma_1(\mathbf{r}'') \equiv \int_{S_t} \tilde{G}^{-1}(\mathbf{r}'';\mathbf{r}')dS(\mathbf{r}'), \tag{21}$$

$$\sigma_\Phi(\mathbf{r}'') \equiv \int_{S_t} \tilde{G}^{-1}(\mathbf{r}'';\mathbf{r}')V_\Phi(\mathbf{r}')dS(\mathbf{r}'), \tag{22}$$

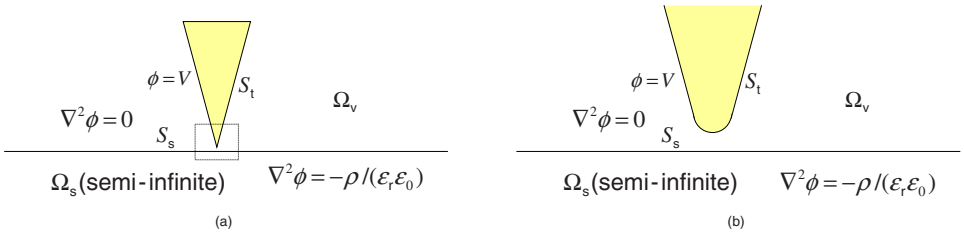

FIG. 2. (Color online) (a) Schematic of the electrostatic boundary value problem simplified by (i) neglecting the cantilever and (ii) assuming the sample to be semi-infinite. (b) Magnification of a region of (a) in proximity to the tip apex [*schematically* shown in a box in (a)].

$$\sigma_\Sigma(\mathbf{r}'') \equiv \int_{S_t} \tilde{G}^{-1}(\mathbf{r}'';\mathbf{r}')V_\Sigma(\mathbf{r}')dS(\mathbf{r}'), \tag{23}$$

$$\sigma_\rho(\mathbf{r}'') \equiv \int_{S_t} \tilde{G}^{-1}(\mathbf{r}'';\mathbf{r}')V_\rho(\mathbf{r}')dS(\mathbf{r}'). \tag{24}$$

To take into account the time dependence of σ due to that of V, we can substitute Eq. (1) into Eq. (20) to find

$$\sigma(\mathbf{r}'',t) = \sigma_{\mathrm{dc}}(\mathbf{r}'') + \sigma_{\mathrm{ac}}(\mathbf{r}'')\sin(\omega t), \tag{25}$$

where for all points on S_t,

$$\sigma_{\mathrm{dc}} = V_{\mathrm{dc}}\sigma_1 - \sigma_\Phi - \sigma_\Sigma - \sigma_\rho, \tag{26}$$

$$\sigma_{\mathrm{ac}} = V_{\mathrm{ac}}\sigma_1. \tag{27}$$

C. Forces in terms of the Maxwell stress tensor

The total force exerted on the probe tip can be obtained by integrating over S_t the traction associated with the Maxwell stress tensor.[9] The force component along the z direction (set to be parallel to the outward normal of the sample surface) is given by

$$F = \frac{\varepsilon_0}{2}\int_{S_t} E^2 n_z dS = \frac{\varepsilon_0}{2}T(E,E), \tag{28}$$

where E is the electric field magnitude and n_z is the z component of the outward surface normal of S_t. The symmetric bilinear operator $T(\cdot,\cdot)$ is defined as

$$T(u,v) \equiv \int_{S_t} uvn_z dS, \quad \forall\, u,v \in L^2(S_t). \tag{29}$$

Since the cantilever and the probe tip are both conductive, Eq. (28) can be written in terms of σ as

$$F = \frac{1}{2\varepsilon_0}T(\sigma,\sigma). \tag{30}$$

Substituting Eq. (25) into Eq. (30) yields

$$F = F_{\mathrm{dc}} + F_\omega \sin(\omega t) + F_{2\omega}\cos(2\omega t), \tag{31}$$

where

$$F_{\mathrm{dc}} = \frac{1}{2\varepsilon_0}T(\sigma_{\mathrm{dc}},\sigma_{\mathrm{dc}}) + \frac{1}{4\varepsilon_0}T(\sigma_{\mathrm{ac}},\sigma_{\mathrm{ac}}), \tag{32}$$

$$F_\omega = \frac{1}{\varepsilon_0}T(\sigma_{\mathrm{dc}},\sigma_{\mathrm{ac}}), \tag{33}$$

$$F_{2\omega} = -\frac{1}{4\varepsilon_0}T(\sigma_{\mathrm{ac}},\sigma_{\mathrm{ac}}), \tag{34}$$

which will take the place of their counterparts in the model of a simple capacitor: Eqs. (6)–(8).

D. Nullifying condition of KPFM

From Eq. (33), the nullifying condition $F_\omega = 0$ according to the KPFM imaging mechanism is equivalent to

$$T(\sigma_{\mathrm{dc}},\sigma_{\mathrm{ac}}) = 0.$$

Solving V_{dc} from the above equation leads to the signal that the KPFM would register as the "surface potential" for the particular probe-sample configuration.

Substituting Eqs. (26) and (27) into Eq. (33) yields

$$F_\omega = \frac{V_{\mathrm{ac}}\sin(\omega t)}{\varepsilon_0}T(\sigma_1, V_{\mathrm{dc}}\sigma_1 - \sigma_\Phi - \sigma_\Sigma - \sigma_\rho). \tag{35}$$

Hence, $F_\omega = 0$ implies

$$V_{\mathrm{dc}} = \frac{T(\sigma_1, \sigma_\Phi + \sigma_\Sigma + \sigma_\rho)}{T(\sigma_1,\sigma_1)} \equiv V_{\mathrm{KPFM}}. \tag{36}$$

Equation (36) states that the KPFM signal V_{KPFM} is a *linear functional* of the sources Φ, Σ, and ρ.

E. Example predictions

Judging from their spacings from the sample (and thus the electrostatic forces they exert thereupon) and for the sake of simplicity, only the tip apex and the conical portion of the probe will be included in the subsequent numerical treatment while the cantilever is neglected, as shown in Fig. 2(a) (the tip apex radius of curvature, the cone height, and the cantilever length are on the orders of 40 nm, 15 μm, and 100 μm, respectively). A magnification for the region in proximity to the tip apex is shown in Fig. 2(b).

For the first set of examples for the forward problem solution, we choose two dielectric samples, each of which contains a surface dipole layer of $\Phi = 1$ V over a square and 0 otherwise, as shown in Figs. 3(a) and 3(c). The side of the square in Fig. 3(a) is 1.75 times the tip radius of curvature, whereas that of the square in Fig. 3(c) is 17.5 times (i.e., one order larger than) the tip radius of curvature. In addition, these samples are assumed to have no other sources to interact with the probe. Hence, the surface potentials measured by KPFM, V_{KPFM}, especially the second one, are expected to be faithful to the true potential Φ.

The predicted KPFM images are shown in Figs. 3(b) and 3(d). The shapes of the "measured" potential inhomogeneity do resemble the true surface potential; however, the measured potential values differ from the true values by *at least*

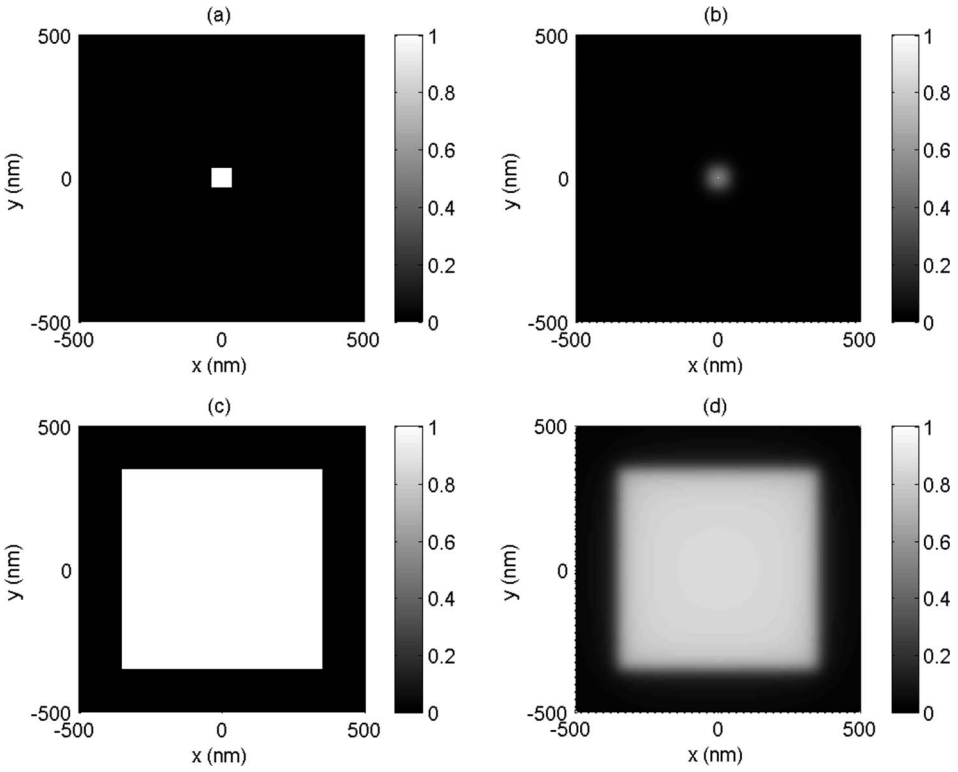

FIG. 3. [(a) and (c)] Prescribed surface dipole density (true surface potential) Φ of samples with dielectric constant $\varepsilon_r=30.0$ with no trapped charge distributions. $\Phi=1$ V over a square centered at (0,0) with a side of (a) 70 nm, or (c) 700 nm, and 0 otherwise. [(b) and (d)] Predicted KPFM image of these samples. The KPFM probe tip radius of curvature is taken to be 40 nm, the tip total length is 15 μm, the tip half conical angle is 15°, and the tip-sample separation is 15 nm. The maximum predicted V_{KPFM} [the value at (0,0)] are (b) 0.46 V and (d) 0.85 V, so that the *minimum* pointwise errors of the surface potential are 54% and 15%, respectively. If the pixel shown in (a) is used as the interpolation function for Φ, then a typical component of the discrete response function, $[R_\Phi^d]_{ij}$, equals the predicted KPFM intensity at point $(x,y)=(i\Delta,j\Delta)$ in (b).

54% and 15% for these two cases. This can be attributed to the long-range characteristic of the Coulombic force, the consequence of which is that the portion of the sample surface outside the square also participates significantly in the interaction with the probe tip. As a result, the KPFM is registering a *weighted average* of the sample surface potential (in this case, weighted averages of 1 and 0 V), leading to this instrumental error.

In the second set of examples, we choose dielectric samples containing a surface charge layer, as shown in Figs. 4(a) and 4(d), where the sizes of the charged areas are the same as those in Figs. 3(a) and 3(c), respectively. The single layer potentials on the surfaces due to these charges in the *absence* of any instrument [literally surface potential], Eq. (15) for $\mathbf{r}' \in S_s$) are plotted in Figs. 4(b) and 4(e), respectively, which are assumed to be what an *ideal* instrument would register. The predicted KPFM images are shown in Figs. 4(c) and 4(f), from which one can also see the broadening effect for small areas of charges; moreover, the errors of KPFM-measured potential values (referenced to the surface potentials) at the centers are also as large as 45% and 10%, respectively.

Finally, the effect of the interior charge distribution ρ is similar to that of the surface charge distribution Σ since both of them enter the boundary integral equation [Eq. (12)] with the same kernel $G(\mathbf{r}-\mathbf{r}')$ [see Eqs. (15) and (16)]. Hence, the counterpart study for the effect of ρ is omitted for conciseness.

F. Convolution relation

Equation (36) is the solution to the forward problem for a particular tip-sample configuration. To write the entire KPFM image in terms of the sample sources to facilitate further analysis, we will follow the treatment in Ref. 7 to decompose a typical position vector $\mathbf{r} \in S_t$ as

$$\mathbf{r} = \mathbf{r}_t + \mathbf{r}^*, \tag{37}$$

where $\mathbf{r}_t=(x_t,y_t,0) \in S_s$ is the nominal probe tip position, defined as the tip apex *projected* onto the sample surface S_s.

The primary unknown of Eq. (12), σ, can now be written as $\sigma(\mathbf{r}^*;\mathbf{r}_t,t)$, and all the integrations over S_t with respect to $\mathbf{r}$ can now be written as integrations over $\mathbf{r}^*$, while the dependence of the probe tip position $\mathbf{r}_t$ becomes explicit.

As a consequence, the KPFM signal $V_{\mathrm{KPFM}}(x_t,y_t)$ can be expressed by rewriting Eq. (36) as linear combinations of convolutions

$$V_{\mathrm{KPFM}} = \Phi * R_\Phi + \Sigma * R_\Sigma + [\rho * R_\rho]_{z_t=0}, \tag{38}$$

where the first two $*$'s are two-dimensional convolutions with respect to (x_t,y_t), while the last $*$ is a three-dimensional convolution with respect to (x_t,y_t,z_t). The response functions R_Φ, R_Σ, and R_ρ are defined as

$$R_\Phi(\mathbf{r}_t) \equiv T[\sigma_1, s_\Phi(\cdot;\mathbf{r}_t)]/T(\sigma_1,\sigma_1), \tag{39}$$

$$R_\Sigma(\mathbf{r}_t) \equiv T[\sigma_1, s_\Sigma(\cdot;\mathbf{r}_t)]/T(\sigma_1,\sigma_1), \tag{40}$$

$$R_\rho(\mathbf{r}_t,z_t) \equiv T[\sigma_1, s_\rho(\cdot;\mathbf{r}_t,z_t)]/T(\sigma_1,\sigma_1), \tag{41}$$

where

$$s_\Phi(\mathbf{r}^*;\mathbf{r}_t) \equiv \frac{\varepsilon_r}{2\pi(\varepsilon_r+1)} \int_{S_t} \tilde{G}^{-1}(\mathbf{r}^*;\mathbf{r}^{**}) z^{**} \times [(x_t+x^{**})^2 + (y_t+y^{**})^2 + (z^{**})^2]^{-3/2} dS(\mathbf{r}^{**}), \tag{42}$$

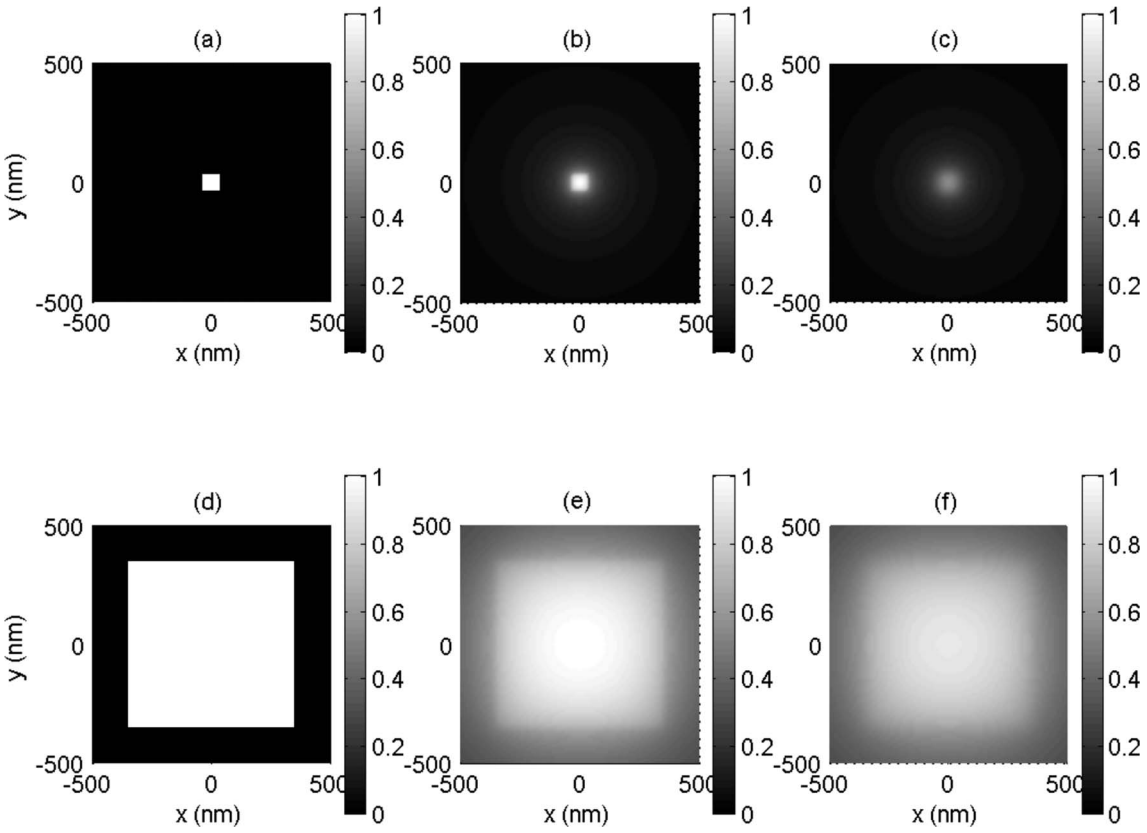

FIG. 4. [(a) and (d)] Contour plots of prescribed surface charge densities Σ with supports as pixels with dimensions $\Delta \times \Delta$, where $\Delta = 70$ nm and 700 nm, respectively. For each case, Σ equals some positive constant over the square and 0 otherwise. [(b) and (e)] The single layer potentials on the sample surface (surface potential) due to the charges in (a) and (d) [Eq. (15) for $\mathbf{r}' \in S_s$], respectively. In both cases, the tip is *absent*. The potentials are normalized so that the maximum values are 1 V. [(c) and (f)] Predicted KPFM images due to charges described in (a) and (d), respectively. The experimental setup and the sample property are the same as those in Fig. 3. The potential values at the centers of the squares of (c) and (f) are 0.55 and 0.90 V, respectively. If the pixel shown in (a) is used as the interpolation function for Σ, then a typical component of the discrete response function, $[R_\Sigma^d]_{ij}$, equals the predicted KPFM intensity at point $(x,y)=(i\Delta, j\Delta)$ in (c).

$$s_\Sigma(\mathbf{r}^*;\mathbf{r}_t) \equiv \frac{1}{2\pi(\varepsilon_r+1)} \int_{S_t} \tilde{G}^{-1}(\mathbf{r}^*;\mathbf{r}^{**}) \times [(x_t+x^{**})^2 + (y_t+y^{**})^2 + (z^{**})^2]^{-1/2} dS(\mathbf{r}^{**}), \tag{43}$$

$$s_\rho(\mathbf{r}^*;\mathbf{r}_t,z_t) \equiv \frac{1}{2\pi(\varepsilon_r+1)} \int_{S_t} \tilde{G}^{-1}(\mathbf{r}^*;\mathbf{r}^{**}) \times [(x_t+x^{**})^2 + (y_t+y^{**})^2 + (z_t+z^{**})^2]^{-1/2} dS(\mathbf{r}^{**}). \tag{44}$$

Here, we have extended the definition of ρ such that $\rho(x,y,z)=0, \forall z>0$.

One of the response functions, R_Φ, has the property that

$$\int_{S_s} R_\Phi(\mathbf{r}_t) dS(\mathbf{r}_t) = \frac{\varepsilon_r}{\varepsilon_r+1}. \tag{45}$$

Hence, for a conductive sample for which $\varepsilon_r \to \infty$, the above integral tends to unity. Furthermore, a conductive sample implies $\Sigma=0$ and $\rho=0$; thus, Eq. (38) becomes a weighted average of Φ, as has also been reported by Ref. 6.

IV. DATA INCOMPLETENESS OF THE INVERSE PROBLEM

While the forward problem of predicting KPFM images from dielectric sample properties is a classical potential problem, solving the responsible sample properties from such images is an inverse problem with insufficient data. The primary insufficiency comes from the fact that for a particular sample, the surface dipole Φ, the surface trapped charge Σ, and the interior trapped charge ρ contribute to the overall Coulombic interaction simultaneously, and their contributions are difficult to isolate from one another. As a result, without further information there will be no unique solution given a particular image.

To overcome this difficulty, one needs a more detailed description of the sample properties in order to deduce more equations or less unknowns. For example, the interior charge contribution to the image can be absorbed in the surface charge contribution term by assuming that the detectable charges are distributed close to the surface. The justification is that KPFM, being a *surface* characterization technique, is usually not expected to be able to register the charge variations *inside* the sample due to the unavoidable thermal noises.

Another incompleteness comes from the fact that only a

subset of the sample surface is imaged, but sources (charges/dipoles) outside the imaging area also contribute to the overall Coulombic interaction. This incompleteness will be overcome in the next section when we implicitly introduce periodic assumption of the source in order to perform the discrete Fourier transform.

V. DECONVOLUTION ALGORITHM FOR TWO-DIMENSIONAL DIPOLE OR CHARGE DISTRIBUTIONS

If the sample of interest can be modeled as having either only a surface dipole layer distribution Φ or only a surface charge layer distribution Σ that is responsible for the Coulombic interaction with the probe tip, then there remains only one term on the right hand side of Eq. (38) (either the first term or second term, correspondingly), and Eq. (38) becomes a one-to-one mapping from the source to the image, allowing one to solve for the source from the image via deconvolution.

Such a deconvolution algorithm was first proposed by Strassburg *et al.*[7] to solve for the surface potential variations of flat conductive samples. They implemented it for the special case of one-dimensional surface potential variation, i.e., the case in which the surface potential is a function of only one Cartesian coordinate. We have generalized this algorithm for dielectric samples and performed, for the first time, a two-dimensional deconvolution study on a KPFM image to solve for the sample's surface charge density.

A. Discrete convolution relation

The expression for the KPFM signal, Eq. (36) or (38), is a continuous function of the nominal probe tip position (x_t, y_t), whereas the pixels of the KPFM image are measurements at only a *discrete* set of sampling points. Thus, at the same level of interpolation accuracy, we can interpolate the true surface sources (Φ and/or Σ) with piecewise constant functions defined over pixels centered at these sampling points.

The following derivations will be specialized to the case of solving for Σ while assuming $\Phi=0$ and $\rho=0$. The case of solving for Φ by assuming $\Sigma=0$ and $\rho=0$ is similar.

We assume that there are $N\times N$ (N is an even number) grid points $(x_t^i, y_t^j), i,j=0,1,\ldots,(N-1)$, with spacings Δ along both the x and y directions; then, the surface charge Σ can be written as

$$\Sigma(x_t,y_t)=\sum_{i=0}^{N-1}\sum_{j=0}^{N-1}\Sigma_{ij}^d b(x_t-x_i,y_t-y_j), \tag{46}$$

where the pixel function b is defined as

$$b(\xi,\eta)\equiv\begin{cases}1 & |\xi|\leqslant\Delta/2 \text{ and } |\eta|\leqslant\Delta/2\\ 0 & \text{otherwise.}\end{cases} \tag{47}$$

The Σ_{ij}^d's are unknown coefficients to be determined via the deconvolution.

In the case of $\Phi=0$ and $\rho=0$, substituting Eq. (46) into Eq. (38) yields the expressions for the pixel intensities,

$$K_{mn}\equiv V_{\mathrm{KPFM}}(x_t^m,y_t^n)=\sum_{i=0}^{N-1}\sum_{j=0}^{N-1}\Sigma_{ij}^d[R_\Sigma]_{m-i,n-j}$$

$$=[\Sigma^d * R_\Sigma^d]_{mn},\quad m,n=0,1,\ldots,(N-1), \tag{48}$$

where $x_t^m\equiv m\Delta$, $y_t^n\equiv n\Delta$, and the discrete response function R_Σ^d is defined as the convolution of the continuous response function and the pixel function

$$[R_\Sigma^d]_{ij}\equiv[R_\Sigma * b](x_t^i,y_t^j),\quad i,j=-N/2,\ldots,N/2. \tag{49}$$

The components of R_Σ^d in Eq. (48) with indices outside the range of $[-N/2,N/2]^2$ are defined by shifting either or both indices by an integer multiple of N to render the indices in that range. For example, $[R_\Sigma^d]_{0,N-1}\equiv[R_\Sigma^d]_{0,-1}$.

Using the convolution theorem, the discrete Fourier transform (denoted $\mathcal{F}$) of Eq. (48) is

$$\mathcal{F}K=(\mathcal{F}\Sigma^d)(\mathcal{F}R_\Sigma^d). \tag{50}$$

Equation (50) will be the basis of the deconvolution algorithm.

B. Computing the discrete response function

The discrete response function $[R_\Sigma^d]_{ij}$ is defined in Eq. (49) via its continuous counterparts. However, if one has set up the computational facility for the forward problem, the response function can be directly obtained by assuming a pixel source located at $(i,j)=(0,0)$, i.e., we input Σ such that

$$\Sigma(x_t,y_t)=b(x_t,y_t) \tag{51}$$

or, equivalently,

$$\Sigma_{ij}^d=\delta_{i0}\delta_{j0}, \tag{52}$$

where δ is the Kronecker delta; then, Eq. (48) becomes

$$K_{mn}=[R_\Sigma^d]_{mn}. \tag{53}$$

Thus, one can compute R_Σ^{mn} by solving a corresponding forward problem. This forward problem is defined by substituting Eq. (51) and $\Phi=0$, $\rho=0$ in Eq. (12) and placing the tip at (x_t^m,y_t^n). An example calculation is given in Fig. 4(c) for the pixel that we will use [Fig. 4(a)] for the deconvolution in Sec. V D. It can be seen that a localized source in Fig. 4(a) becomes a broadened response, as shown in Fig. 4(c), due to the finite curvature of the probe tip. The counterpart for R_Φ^d which is related to $R_\Phi * b$ is shown in Fig. 3(b) for the pixel source of surface dipole given in Fig. 3(a).

C. Enforcing the sample electric neutrality

To guarantee the electric neutrality while maintaining the consistency of the deconvolution algorithm, $[\mathcal{F}K]_{00}$ is forced to be zero, so that $[\mathcal{F}\Sigma^d]_{00}$ is also zero.

This preprocessing is consistent with the observation that the integral

$$\int_{S_s}R_\Sigma(\mathbf{r}_t)dS(\mathbf{r}_t) \tag{54}$$

diverges, i.e., $[\mathcal{F}R_\Sigma](0,0)=\infty$, where $\mathcal{F}$ denotes the Fourier transform. As a result, from the convolution theorem, if $[\mathcal{F}V_{\mathrm{KPFM}}](0,0)<\infty$, then $[\mathcal{F}\Sigma](0,0)=0$, which automatically satisfies the electric neutrality. In the discrete counter-

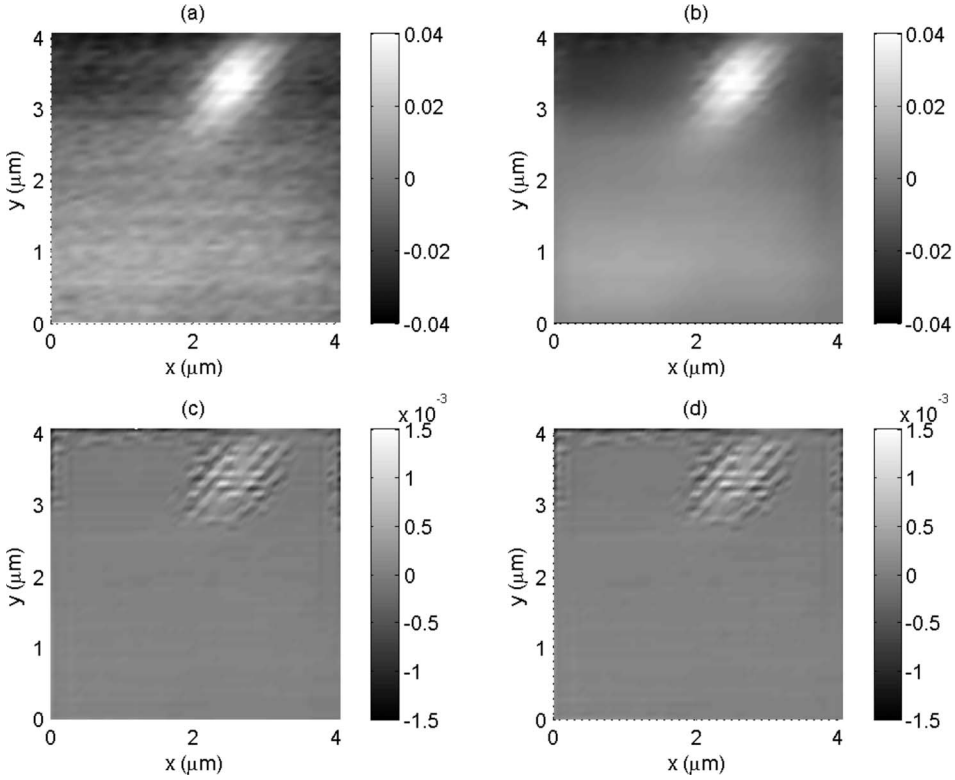

FIG. 5. (a) Raw (Ref. 10) and (b) noise-filtered (with the Wiener filter) KPFM images on a gadolinia-doped ceria thin film. The units of both are V. The probe is 15 μm long and has a half conical angle of 15°. The probe tip radius is 40 nm. The tip-sample separation is 15 nm. The dielectric constant ε_r is 30.0. The spacing of the sampling points is Δ=70 nm. The number of sampling points in either direction is 59. [(c) and (d)] Contour plots of the reconstructed surface charge density Σ from (b) via deconvolution. The unit is e/nm^2, where e is the elementary charge. Before deconvolution, the filtered data are extended with zeros to render (c) 128×128 or (d) 256×256 data points to mitigate the edge effect. The discrete response functions are arrays of the respective sizes.

part, however, $[\mathcal{F}R_\Sigma^d]_{00}$ is a finite number, so that the electric neutrality has to be explicitly enforced.

D. Sample application to experimental data

We will apply the deconvolution algorithm for a KPFM image obtained by Lee[10] from experiments shown in Fig. 5(a). The sample is a gadolinia-doped ceria (GDC) thin film which is a popular material used as electrolyte in solid oxide fuel cells. This thin film has a thickness of 50–100 nm. It was fabricated by sputtering $Gd_{0.2}Ce_{0.8}$ alloy (Kurt Lesker Co.) on a 200 nm thick Pt layer (serving as a reference electrode), which had been sputtered on a silicon nitride film. The $Gd_{0.2}Ce_{0.8}$ film was then oxidized in air at 650 °C for 5 h.

The surface modulation, topographic measurement, and the surface potential measurement on the GDC film were performed in ambient condition at room temperature using the same instrument, Molecular Imaging Inc. 's PicoPlus II AFM with a probe coated with highly boron-doped diamond. In addition, commercial radio frequency lock-in amplifiers with dedicated circuitry were set up for imaging the surface potential using the KPFM mechanism described in Sec. II A.

Before being imaged, the sample surface was modulated by placing the probe tip *in contact* with the sample and applying a positive dc voltage on the tip (referenced to the Pt layer) to facilitate some chemical reaction. After that, the topography and the surface potential were measured in the contact mode and the amplitude modulation mode, respectively. Such measurements were performed for each scan line to generate maps of topography and surface potential.

As a result of the surface modulation, a peak centered at the former contact region is observed in the subsequent KPFM image, indicating charge concentration in this region compared to the rest of the imaging area. In order to obtain the surface charge density from the KPFM image, the deconvolution algorithm will be used.

However, since this is a set of raw data, there would be instrument noise superposed to the measured V_{KPFM}. This noise is sensitive to deconvolution operations; hence, we apply the Wiener filter[11] *prior to* the subsequent treatment.

Furthermore, to mitigate the edge effect due to the implied two-dimensional periodic assumption of both the source and the measurement (implied by the discrete Fourier transform and the discrete convolution relation), we have extended zeros to the filtered data set. For the ideal case of a response function with compact support, the number of zeros needed in each direction is, according to Ref. 13, Chap. 13, at least half the maximum width of the response function in that direction. However, the response function R_Σ not only lacks compact support but also decays to zero slowly. Thus, we cannot use the rule suggested by Ref. 13. Instead, we try to extend more zeros in each direction than there are number of data points in the same direction of the original data set.

For concreteness, the raw data[10] has 59×59 data points. We have examined the effects of extending zeros to render 128×128 or 256×256 data points (N=128 or 256, respectively). The corresponding discrete response functions have nonzero values in all entries. According to Eq. (49), their indices are in the range of $[-64,64]^2$ or $[-128,128]^2$, respectively. After the deconvolution, only those entries in Σ^d corresponding to the raw data (rather than the zeros) are retained.

The surface charge density Σ's obtained using this algorithm with the two choices of N's are plotted in Figs. 5(c) and 5(d), which do not appear to be significantly different to the naked eye. This means that zero extending to whether

128×128 or 256×256 data points does not lead to significant differences. For concreteness, let $[\Sigma_{128}]$ and $[\Sigma_{256}]$ denote the solutions at the grid points corresponding to the cases of $N=128$ and 256, respectively. The root mean square of the entries of the difference $[\Sigma_{256}]-[\Sigma_{128}]$ is $1.5\times10^{-5}\ e/\mathrm{nm}^2$, whereas that of $[\Sigma_{256}]$ is $2.0\times10^{-4}\ e/\mathrm{nm}^2$, giving a measure of the relative difference of the two solutions of 7.4%. Further convergence analysis may be necessary for determining the minimum size of data points N required for the deconvolution.

From Figs. 5(c) and 5(d), we can see that the Gaussian-like intensity variations in Fig. 5(a) become localized sources in Figs. 5(c) and 5(d). The surface charge density shown in Fig. 5(c) or 5(d) is a solution to the inverse problem, which is a more appropriate description for samples of this kind compared to the raw image with (broadened) "CPD" values ill defined for dielectric samples.

ACKNOWLEDGMENTS

The first author would like to express his thanks to Minhwan Lee and Wonyoung Lee of the Rapid Prototyping Laboratory at Stanford University for helpful discussions about KPFM as used in laboratories. The authors also thank the reviewer for the extensive and detailed comments and suggestions. This research has been funded by the Global Climate and Energy Project at Stanford University.

APPENDIX A: DERIVATION OF THE BOUNDARY INTEGRAL EQUATION

For the boundary value problem shown in Fig. 1, we apply Green's second identity to $\phi(\mathbf{r})$ and $\tilde{G}(\mathbf{r};\mathbf{r}')$ (for some $\mathbf{r}'\in\Omega_v$) in Ω_v to find

$$\int_{\Omega_v}[\tilde{G}(\mathbf{r};\mathbf{r}')\nabla^2\phi(\mathbf{r})-\phi(\mathbf{r})\nabla_{\mathbf{r}}^2\tilde{G}(\mathbf{r};\mathbf{r}')]d\Omega(\mathbf{r}) = -\int_{S_t\cup S_s}\left[\tilde{G}(\mathbf{r};\mathbf{r}')\frac{\partial\phi_v(\mathbf{r})}{\partial\mathbf{n}}-\phi_v(\mathbf{r})\frac{\partial\tilde{G}(\mathbf{r};\mathbf{r}')}{\partial\mathbf{n}_{\mathbf{r}}}\right]dS(\mathbf{r}), \tag{A1}$$

where $\mathbf{n}$ and $\mathbf{n}_{\mathbf{r}}$ denote outward normal of either the sample or the probe tip, which is opposite to the outward normal of Ω_v, which accounts for the minus sign on the right hand side of Eq. (A1).

On the other hand, applying Green's second identity of $\phi(\mathbf{r})$ and $G(\mathbf{r}-\mathbf{r}')$ in Ω_s yields

$$\int_{\Omega_s}[G(\mathbf{r}-\mathbf{r}')\nabla^2\phi(\mathbf{r})-\phi(\mathbf{r})\nabla_{\mathbf{r}}^2G(\mathbf{r}-\mathbf{r}')]d\Omega(\mathbf{r}) = \int_{S_s}\left[G(\mathbf{r}-\mathbf{r}')\frac{\partial\phi_s(\mathbf{r})}{\partial\mathbf{n}}-\phi_s(\mathbf{r})\frac{\partial G(\mathbf{r}-\mathbf{r}')}{\partial\mathbf{n}_{\mathbf{r}}}\right]dS(\mathbf{r}). \tag{A2}$$

The boundary integral equation [Eq. (12)] can then be obtained in three steps: substituting the partial differential equation [Eq. (9)] and the boundary conditions [Eqs. (10) and (11)] into Eqs. (A1) and (A2), using the resultant equations to eliminate ϕ_v and ϕ_s and their normal derivatives at S_s, and letting $\mathbf{r}'$ approach S_t [so that $\phi(\mathbf{r}')$ tends to the applied voltage V due to the continuity of the potential ϕ across S_t].

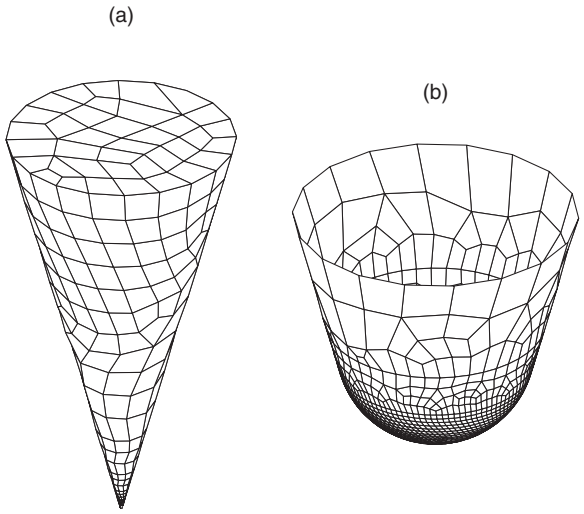

FIG. 6. (a) Typical surface mesh of the probe tip to be used for the boundary element calculation. (b) A magnified view of the mesh on the apex.

APPENDIX B: IMPLEMENTING THE BOUNDARY ELEMENT METHOD FOR SOLVING THE BOUNDARY INTEGRAL EQUATION

To numerically solve the boundary integral equation [Eq. (12)] or, generally,

$$\int_{S_t}\tilde{G}(\mathbf{r};\mathbf{r}')\sigma(\mathbf{r})dS(\mathbf{r})=f(\mathbf{r}'),\quad \forall\,\mathbf{r}'\in S_t, \tag{B1}$$

for some known function f, we first discretize the probe tip surface S_t with boundary elements, usually triangles or quadrilaterals. We choose the eight-node serendipity quadrilateral elements (Ref. 12, Chap. 3) for their capability to represent quadratic functions. The element size on the tip apex is set to be $0.06R$, where R is the tip radius of curvature, whereas the element is coarser for positions farther away from the probe tip. For a calculation in this paper, we input $R=40$ nm, tip total length of 15 μm, and tip half conical angle of 15°. The corresponding mesh has 6959 nodes (see Fig. 6).

Then, we interpolate the unknown σ in terms of the associated shape functions,

$$\sigma(\mathbf{r})=\sum_{A=1}^{n}\sigma_A N_A(\mathbf{r}). \tag{B2}$$

Usually, but not necessarily, the shape functions satisfy $N_A(\mathbf{r}_B)=\delta_{AB}$, $A,B=1,\ldots,n$, where $\mathbf{r}_B$ is the position vector of the Bth node and δ is the Kronecker delta.

The integral equation [Eq. (B1)] is then collocated to all the nodal points by setting $\mathbf{r}'=\mathbf{r}_A$, $A=1,\ldots,n$,

$$\sum_{B=1}^{n}\left[\int_{S_t}\tilde{G}(\mathbf{r};\mathbf{r}_A)N_B(\mathbf{r})dS(\mathbf{r})\right]\sigma_B=f(\mathbf{r}_A),\quad A=1,\ldots,n, \tag{B3}$$

to obtain a set of n linear simultaneous equations.

The coefficient matrix and the right hand side vector can be assembled from element-pair contributions, where the regular and weakly singular integrals are computed using the methods described in Chap. 6 of Ref. 12. The coefficient matrix is then LU decomposed. After that, the right hand side vector is used with the LU decomposition to solve for the entries in $[\sigma]$ with a process called *backsubstitution* (Ref. 13, Chap. 2).

Note that the coefficient matrix does not depend on the *lateral* position of the probe tip, hence, the coefficient matrix is the same for the *entire scan* at a constant tip-sample separation. Thus, for each additional tip-sample configuration corresponding to an additional right hand side vector, one only needs to perform one more backsubstitution.

[1] M. Nonnenmacher, M. P. O'Boyle, and H. K. Wickramasinghe, Appl. Phys. Lett. **58**, 2921 (1991).
[2] C. Loppacher, U. Zerweck, and L. M. Eng, Nanotechnology **15**, S9 (2004).
[3] Y. Rosenwaks, R. Shikler, Th. Glatzel, and S. Sadewasser, Phys. Rev. B **70**, 085320 (2004).
[4] H. Hoppe, T. Glatze, M. Niggemann, A. Hinsch, M. Ch. Lux-Steiner, and N. S. Sariciftci, Nano Lett. **5**, 269 (2005).
[5] V. Palermo, M. Palma, Ž. Tomović, M. D. Watson, R. Friedlein, K. Müllen, and P. Samori, ChemPhysChem **6**, 2371 (2005).
[6] H. O. Jacobs, P. Leuchtmann, O. J. Homan, and A. Stemmer, J. Appl. Phys. **84**, 1168 (1998).
[7] E. Strassburg, A. Boag, and Y. Rosenwaks, Rev. Sci. Instrum. **76**, 083705 (2005).
[8] M. Lee, W. Lee, and F. B. Prinz, Nanotechnology **17**, 3728 (2006).
[9] J. D. Jackson, *Classical Electrodynamics* (Wiley, New York, 1998).
[10] M. Lee, Ph.D. thesis, Stanford University, 2008.
[11] A. K. Jain, *Fundamentals of Digital Image Processing* (Prentice-Hall, Englewood Cliffs, NJ, 1989).
[12] G. Beer, *Programming the Boundary Element Method: An Introduction for Engineers* (Wiley, Chichester, 2001).
[13] W. H. Press, S. A. Teukolsky, W. T. Vetterling, and B. P. Flannery, *Numerical Recipes in FORTRAN: The Art of Scientific Computing* (Cambridge, New York, 1992).